A Combined Rigid-Soft Thruster Based on Jetting Propulsion

Christoph Stoeffler[1⋆], Adriano del Río[1], René Sonntag[2], Florian Hoffmann[2],
Shivesh Kumar[3] and Frank Kirchner[1]

***Abstract*— A new underwater thrust device is proposed in this work that makes use of a soft outer structure in combination with a parallel linkage and driven by a classical actuator. By merging soft and rigid parts, we hope to increase the performance of pulsed jet propulsion that plays a crucial role in attitude control for AUVs. But also simpler models for design and control can be applied by this approach. A specific linkage design for actuation, along with two different soft structures (mantles) are introduced and evaluated in experiments which indicate efficient thrust creation. *Particle Image Velocimetry* (PIV) experiments show the formation of vortex rings that suggest efficient propulsion, whereby the wider and more flexible mantel is characterized by higher momentum and thrust.**

I. INTRODUCTION & OVERVIEW

Soft robotics is widely inspired by biological systems and challenged by them in terms of benchmark examples. Nature's capabilities are often beyond feasible current technical solutions, hence, it is difficult for soft systems to outperform their biological antetypes. Simultaneously, it is hard to compete with classical rigid robots with high frequency feedback control, raising questions as to why one would use soft systems at all - see [1]. Soft robots have widely been used for underwater propulsion in different locomotion modes [2]. We believe that soft systems are best suited when included as an integrative part of a larger technical solution. In this work, we propose a biologically inspired underwater thruster that uses a rigid linkage for actuation in combination with a passive soft structure. We aim for the important property of pulsed thrust for underwater vehicles, as highlighted and exploited by Krieg and Mohseni; a crucial element for underwater attitude control, like in [3] and [4]. Using soft structures within this context is not new (e.g. [5], [6]) and detailed models of the structural dynamics and fluid-structure interactions have already been validated e.g. in [7] and [8]. To mimic radial and circular muscles of the mantle in squid-inspired designs, tendon actuation is primarily used or assumed in these works. However, other approaches of soft actuation have been adopted [9]. The overall performance of the design in the latter work highlights several gaps between technological feasibility and performance expectations of soft robotics, as previously mentioned. Thrust creation in squids is often associated with vortex formation in the fluid and the natural frequency of the system. The latter is coupled to turbulent effects, occurring by water ingestion of previous jet cycles, as outlined by [4]. Several challenges remain in the mimicry of muscles [5] and internal parallel linkages have already been proposed as a solution to these challenges [10].

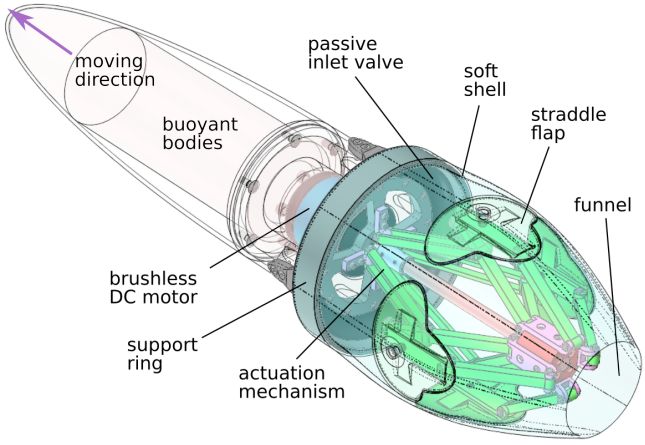

Fig. 1. Model of the design *II* equipped with streamlined body and buoyant. A central motor expands the soft structure via spindle driven linkages to create thrust.

By combining rigid and soft parts, we expect that improvements can be made in terms of propulsive performances, as recently shown by Bujard and others [11]. For this purpose, a soft mantle that allows high deformations and elastic energy storage is combined with a parallel mechanism, used for specific motion initiation and preferable force transmission (Fig. 1). With our design, it is demonstrated that incorporating rigid linkages of optimized geometry into soft structures can create effective thrust. Compared to the aforementioned works, we shifted efforts in creating optimal designs from soft to rigid parts, where the latter are simpler to model and control. Like others, this work aims at creating thrust comparable to squids [12], but compared to e.g. [5] the motion of the soft mantle is more directly controlled. Our design shows to be inherently pressure-tolerant. In a test with more than 8500 actuation cycles under 600 bar and a continuous exposure of the device to at least 450 bar for 22 hours was successful[1]. However, this prototype comes as a tethered device. To make the system autonomous, electronics and batteries would need to be integrated into a potentially bigger float and cast in resin.

[1]: Robotics Group, University of Bremen, Bremen, Germany
[2]: Biomimetics-Innovation-Centre, City University of Applied Sciences, Bremen, Germany
[3]: German Research Center for Artificial Intelligence, Bremen, Germany
⋆: Corresponding author - christoph.stoeffler@dfki.de

[1]pressure chamber: Dustec up to 1000 bar and a 75 l volume, pressure pump: RSD-Compact 4 kW in combination with Resato Type P160, pressure sensor WIKA Eco-1 with range up to 1000 bar

Two flexible shells of different geometry are designed, adapted, and tested in this work for their functionality. The internal actuation mechanism, after being once optimized, is not altered. In Sec. II we touch upon the design of the thrust device and explain its main features. Additionally, some theoretical considerations are made to reconcile the mantle designs with the actuation e.g. to stay within given strain limits. Following this, simplified thrust computations are carried out in Sec. III, to be revised by experiments mentioned in Sec. IV. To asses our design, we utilized *Particle Image Velocimetry* (PIV). PIV has been used to measure hydrodynamics of swimming jellyfish and squids and has shown that the formation of vortex rings can be an efficient measure of propulsive performance [13], [14] and [15].

II. SYSTEM DESIGN

An overview of the thrust device can be seen in Fig. 1. In this configuration it is equipped with a streamlined head and several buoyant bodies. Key data about the systems is listed in Tab. I. Within the system's interior, a brushless DC motor is installed which drives a centrally located spindle to actuate four constraint pantograph mechanisms that are equally distributed over the mantles circumference. When the spindle nut is pulled towards the motor, a straddling movement of the pantographs widens the soft structure and therefore initiates the filling phase of the mantle. A passive valve behind the motor facilitates the entry of water. The straddle mechanism is actuated up-to or slightly beyond its "locking point" as to have maximal extension in which the peak of elastic energy in the mantle is reached. Finally, water expulsion towards the rear of the vehicle is then introduced and supported by the spindle nut movement away from the motor. In the following section, we provide details on the design mechanism in addition to discussing the static mantle simulation.

TABLE I
DESIGN SPECIFICATIONS OF THE TWO DIFFERENT THRUSTER VERSIONS

structure material		Polylactic
buoyant material		PVC foam - Divincell HCP 30
mantle material		Ecoflex 35 with 5 % thinner
motor		Blue Robotics M200
spindle		helix spindle with 25.4 mm pitch
outer diameter		98 mm
overall length	des. *I*	381 mm
	des. *II*	396 mm
displacement	des. *I*	0.721
	des. *II*	0.731
funnel diameter	des. *I*	76 mm
	des. *II*	45 mm

A. Actuation Mechanism

While there exist many different soft actuators, it was found that utilizing a traditional actuation mechanism was more appropriate for the system in question. This is mainly due to the constraints posed by deep-sea applications that dismiss actuators relying on complex supplementary hardware, high voltages or pneumatic pressure, aside with principles of lower technical maturity - see e.g. [16]. Using a pressure-tolerant BLDC-motor in combination with a parallel mechanism allows a task-oriented design with reasonable complexity and energy efficiency. The final mechanism is depicted in Fig. 2 which shows geometrical details of one of the four identical linkages inside the mantle. To describe its kinematics, a base frame $\{0\}$ is attached at the output shaft of the motor to be seen alongside the end-effector frame $\{E\}$ that connects linkage and mantle via a straddle flap. Forward kinematics $f(\theta) = y$ relate the output coordinate y to the input coordinate θ. In our case, it is a scalar function linking the spindle position θ and the height y of the end-effector. The prescribed coupler curve of the end-effector, as a result of this function, can be seen as dotted line in Fig. 2. Building the time derivative yields

$$\frac{d}{dt}\left(f(\theta(t))\right) = \dot{y}(t) \Leftrightarrow \frac{\partial f}{\partial \theta}\dot{\theta} = \dot{y} \tag{1}$$

omitting the explicit time dependency. Assuming conserved power between input and output gives $F_s = \partial f/\partial\theta F_e$, where F_s and F_e are the spindle and end-effector force, respectively. The derivative $\partial f/\partial\theta$ appears as a transfer function between input and output of the mechanism. In our previous work [17] the mechanism geometry was optimized by means of a genetic algorithm for a predefined extension in y-direction. The fitness function of the algorithm considered

1) a minimization of $\partial f/\partial\theta$
2) least deviation of the trajectory in x-direction
3) least rotation of end-effector frame during motion

By selecting the "fittest" designs among randomly varied geometries, the algorithm returned several optimized geometric parameters, given in table II. For "mutation" of different geometries, a normally distributed probability was applied.

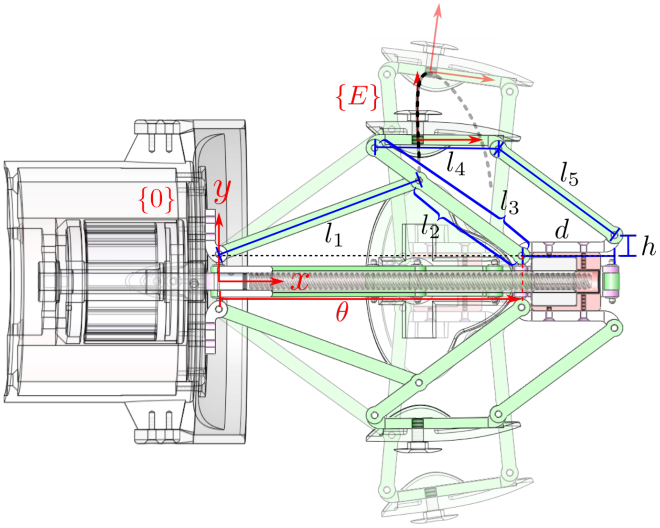

Fig. 2. Actuation mechanism in retracted and extended (greyed) configuration with its geometric parameters. The spindle position θ is input to the linkage and the y-position of $\{E\}$ output to it. Part of the mechanisms coupler curve is depicted as dotted line.

TABLE II

STARTING VALUES AND OUTPUT PARAMETERS OF GEOMETRY OPTIMIZATION. OUTPUTS ARE ROUNDED FOR THE DESIGN PROCESS.

in mm	l_1	l_2	l_3	l_4	l_5	d	h
inp. param.	55.0	22.5	45.0	30.0	45.0	22.5	0.0
opt. param.	62.0	37.0	53.0	36.0	42.0	27.0	6.0

B. Mantle Design and Manufacturing

As the generated thrust is primarily determined by the cyclic expansion and contraction of the flexible mantle, its deformation behavior has been investigated by means of FEA simulations using the CAD-embedded software *Nastran*. The loadcase consists in applying a forced displacement of 12.5 mm in radial direction on the contact area of the straddle flaps and a fixation on the contact area of the support ring, see Fig. 1. This flexible mantle displacement corresponds to the maximal attainable $y-$position of $\{E\}$. Generally, the dynamic motion of the flexible mantle depends on hydrodynamic loads imposed by the ambient fluid, such as in the case of expansion. The overall deformation of the mantel during the mantle expansion is predominantly determined by the intramantel strain and the loading phase was considered therefore as a quasi-static process. The simulations showed that the maximal von Mises stress, σ_{max}, in both shell designs occurs between two shell attachment points of the actuating linkage. Simulation results of both designs can be taken, along with the simulated volumes in inflated and contracted state, V_0 and V_1, respectively, from Tab. III. The corresponding crossectional areas of the funnel A_0 and A_1 in both states are also given. Both cast mantles posses

TABLE III

SIMULATION RESULTS FOR MANTLE EXPANSION

	V_0	V_1	A_0	A_1	σ_{max}
des. *I*	839 cm^3	747 cm^3	40.9 cm^2	45.4 cm^2	0.0542 N/mm^2
des. *II*	854 cm^3	753 cm^3	15.4 cm^2	15.3 cm^2	0.0604 N/mm^2

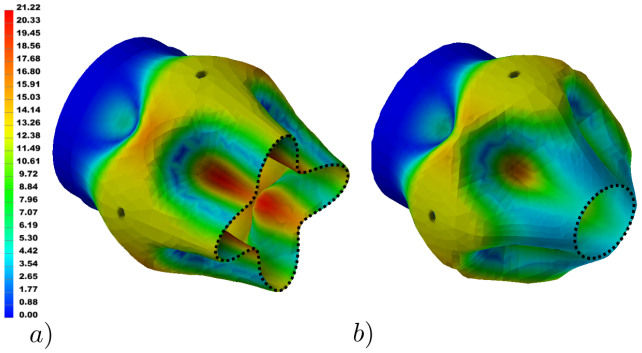

Fig. 3. Results of FEA simulations showing the deformation of the mantle when the actuating linkage is expanded for mantle design *I* (a) and *II* (b). While the shape of the funnel changes visibly in the first design, it maintains its circular shape in the latter.

relative complex geometries with changing thickness over length and circumference to attain good load insertion and specific deformations. This can be accounted for by 3D-printed mold parts limiting the outer and inner surface of the mantle as shown in Fig. 4. A surfacer is applied on the molds to improve surface quality of the final cast. Relative positioning of the three mold parts is achieved by guiding pins and bores which leave a whole in the cast which is furthermore used to clamp the straddle flaps at a defined position onto the mantle (Fig. 1). In an upright position, liquid silicone is injected into the assembled molds at two insertion points and filling is checked via outlet ports on top of the mold. The two different designs of the mantle

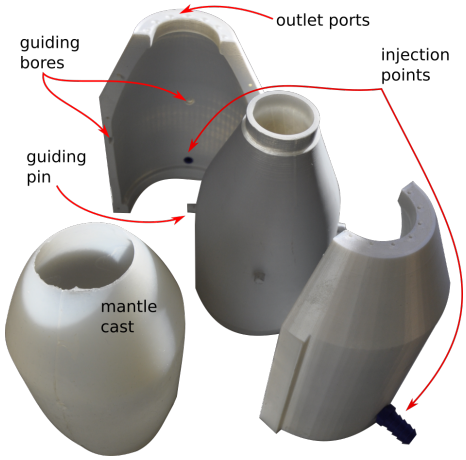

Fig. 4. 3D-printed molds to obtain complex geometries in silicone rubber. A divided outer mold clasps around the inner one and injection occurs from bottom to top to prevent defects.

give rise to different locomotion patterns. Hence, it was also part of our aim to investigate the specific behavior of both designs regarding thrust creation (or locomotion behaviors). For example, when the design *I* possesses a thinner and wider mantle - specifically at its rear - the propulsive mode tend to have locomotion similar to a jelly fish (see e.g. [18]). On the contrary, a thicker mantle with an almost undeformed funnel will have more similarities to squid locomotion, like explained in [12].

III. THRUST PULSE ESTIMATION

In order to provide a realistic description of the present physics in pulsed swimming, one has to consider the inertia, strain and friction forces of the fluid for an immersed structure, as done in [8] for the 2D case. This then requires coupling the domain of structural and fluid dynamics, resulting in a complex set-up of simulation programs. Therefore, we start our considerations simply from a time-dependent momentum equation $p(t) = m(t)u(t)$, where $m(t)$ is the emitted mass of fluid under the velocity $u(t)$. Thrust force is then the time derivative of this equation:

$$F(t) = \frac{\partial}{\partial t}\left(m(t)u(t)\right) \tag{2}$$

Finding meaningful expressions for mass transport and fluid velocity, can be achieved by considering the itramantle

volume $V(t)$ and the funnel area $A(t)$ as time dependent functions. Regarding an incompressible fluid, mass becomes

$$m(t) = \Delta V(t)\rho \tag{3}$$

where $\Delta V(t)$ is the volume change of the cavity from its inflated configuration at time instant t and ρ denotes the waters unchanged density. Mass flow across the funnel then equates to

$$\dot{m}(t) = \Delta \dot{V}(t)\rho \tag{4}$$

$$= u(t)\rho A(t) \tag{5}$$

using the assumption of an average exhaust velocity $u(t)$ over the funnel in (5). This velocity therefore becomes $u(t) = \Delta \dot{V}(t)/A(t)$ what can, together with (4), be inserted into (2), such that

$$F(t) = \frac{\Delta \dot{V}^2(t)\rho}{A(t)} + \Delta V(t)\rho \frac{\Delta \ddot{V}(t)A(t) - \Delta \dot{V}(t)\dot{A}(t)}{A^2(t)} \tag{6}$$

Here, the first term of (6) denotes the forces stemming from the emitted mass flow and the second term arises from accelerated water mass from rest. By linearly interpolating the volume and funnel area of the inflated and deflated mantle structures (Tab. III) by the end-effector position $y(\theta(t))$ and inferring a spindle velocity $\dot{\theta}(t)$, then meaningful functions for $\Delta V(t)$ and $A(t)$ and their time derivatives can be obtained. We preempt some of the experimental results at this point and highlight the specific dependency of our modelling (6) on the spindle velocity profile. From the motor controller a pulse interval of Δt is set what defines the required spindle speed, once the ramp time τ is given - see Fig. 5.

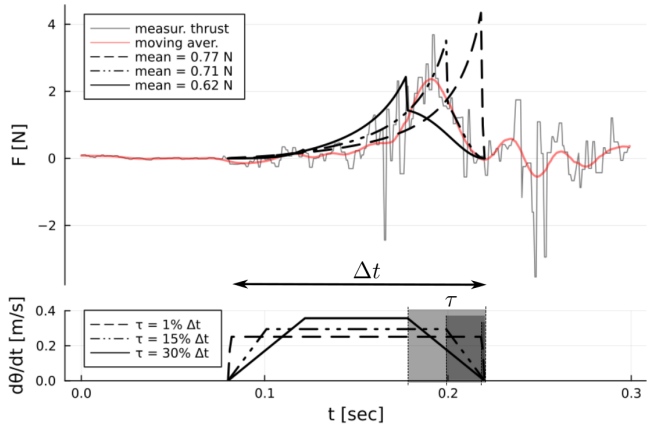

Fig. 5. Top: Measured thrust values of des. *II* (1367 Hz sample rate) interpolated by moving average (n =65) and compared to thrust model for different spindle speed profiles. Bottom: Related spindle speed profiles where τ is the duration of the rising or falling ramp.

A comparison of the theoretical thrust model and the measured data for an arbitrary pulse ($\Delta t = 0.14$) can be seen in Fig. 5, revealing a good approximation for $\tau = 15\,\%$. It is important to note here, that a slight modification of (6) is required in order to obtain meaningful data. Since the mantle accelerates water from rest, the unsteady term in (6) is dominant in the computations. Since the fluid is considered here as a continuum, high negative thrust occurs in the deceleration phase of the spindle, bringing the overall thrust integral to zero. In reality, the accelerated water mass leaves the structure, even though viscous forces are present and observable in negative thrust measurements right after pulses. To account for this effect, the unsteady forces are set to zero in time interval $\Delta t - \tau < t < \Delta t$. The model neglects viscous forces and thereby exceeds the measured values, but can represent partly the effects that are present during thrust pulses. By choosing shorter ramp times (and thereby increasing the acceleration of the spindle), higher average thrusts are given by the model and range to 0.77 N. In contrast, mean values of positive measurement in Fig. 5 reach 0.69 N. If the considered interval is extended and negative thrust measurements are included this value is reduced to 0.27 N.

IV. EXPERIMENTS

In this section, we try to reflect the simple thrust computations of both system configurations by the thrust obtained from force measurements and the flow field around the funnel captured by PIV.

A. Thrust Measurements for several Pulses

For both mantle structures, five measurements with five cyclic thrust pulses each were taken, using a *IMADA ZPS-DPU-500* sensor at 45 Hz. These results are listed in Tab. IV. To our surprise, the design with the wide funnel (design *I*) delivers higher peak thrust and higher thrust for single pulses, what is also discussed in Sec. V. However, for multiple pulses, the narrow funnel showed better average thrust.

TABLE IV
THRUST MEASUREMENT RESULTS OVER SEVERAL PULSES OF BOTH MANTLE DESIGNS

	av. thrust [N]					**av.**
run	1	2	3	4	5	
des. *I*	0.15	0.11	0.15	0.21	0.16	**0.16**
des. *II*	0.2	0.19	0.2	0.2	0.24	**0.21**
	av. peak thrust [N]					**av.**
des. *I*	6.42	6.12	6.8	6.3	5.76	**6.28**
des. *II*	4.08	4.42	4.14	4.3	4.16	**4.22**

A typical profile of thrust measurements from multiple pulses is given in Fig. 6 showing short force impulses over an approximate duration of $\Delta t \approx 0.2$ s. Multiple thrusting leads to volatile force profiles, indicating interference between the separate pulses. While the force peaks can reach up to 7 N, an average thrust over all cycles of 0.2 N was barely exceeded.

B. Particle Image Velocimetry

To perform PIV and thrust measurements the underwater thrust device was mounted in the test section (250×250×1000 mm) of a recirculating flow channel. The water was seeded with neutrally buoyant polyamide particles

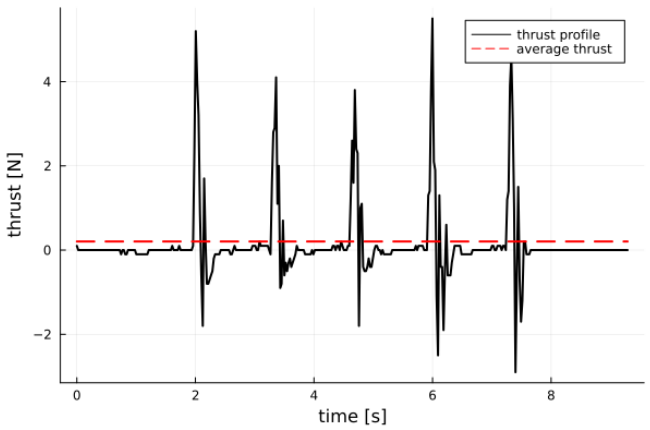

Fig. 6. Thrust profile of test des. *II*, 1st run with five distinct pulses. The loading phase of the mantle is marked by small force registrations starting at $t = 0.75$ s and followed by a thrust profile exceeding 4 N in average. Negative thrust can be observed right after each pulse, increasing in magnitude over the performed cycles.

(57 μm diameter, density 1.03 g/cm^3). A laser[2] light sheet illuminated the horizontal mid plane (250x250 mm) behind the thrust device. Time resolved PIV-images were recorded at 400 fps (interframing time of Δt = 2.5 ms). The high speed camera (Phantom VEO410, Vision Research Inc., NewJersey, USA) was set with a perpendicular view from below on the laser light sheet. Camera and laser pulses were synchronized (Laser Pulse, model 610036, TSI Inc., Shoreview, USA).

To measure thrust, the underwater thrust device was mounted by a rod to a force balance. Its mounting plate was attached to 3 spring steel plates, so the force dependent deflection could be measured with an displacement transducer (HBM W1ELA, Hottinger Brüel & Kjaer GmbH, Darmstadt, Germany) at a sample rate of 100 Hz. For each experiment, a motion cycle was started from a standing position. New recordings were only started when the water in the test section had settled down. For both mantle configurations, 10 cycles of motion were analyzed consisting of 550 images for design *I* and 300 images for design *II*. The PIV analysis was performed with PIVLab 2.59 [19], with standard parameter settings, except: three consecutive correlation passes with successively decreasing sizes of the interrogation area (64×64, 32×32, 24×24) were calculated. Within the software settings, the "Correlation robustness" was set to "extreme" and the "repeat last pass until quality slope = 0.025" was set to active. The data determined for each time step (Δt = 2.5 ms) from separately analyzed cycles ($n = 10$) were averaged and used for further comparison. The vorticity was used to identify vortex rings and the circulation was measured with the software integrated tool at about 0.08 m (behind the thrust device). Circulation Γ of the ring shaped vortex was derived by a closed loop integration of the fluid velocity $\vec{u}$ along the jet main axis, with the simplified line integration, assuming $u_y = 0$ for the upstream

[2]Pegasus PIV-Laser, Nd:YLF, λ = 527 nm, P_{max} = 45 W, New Wave Research Inc., Freemont, USA

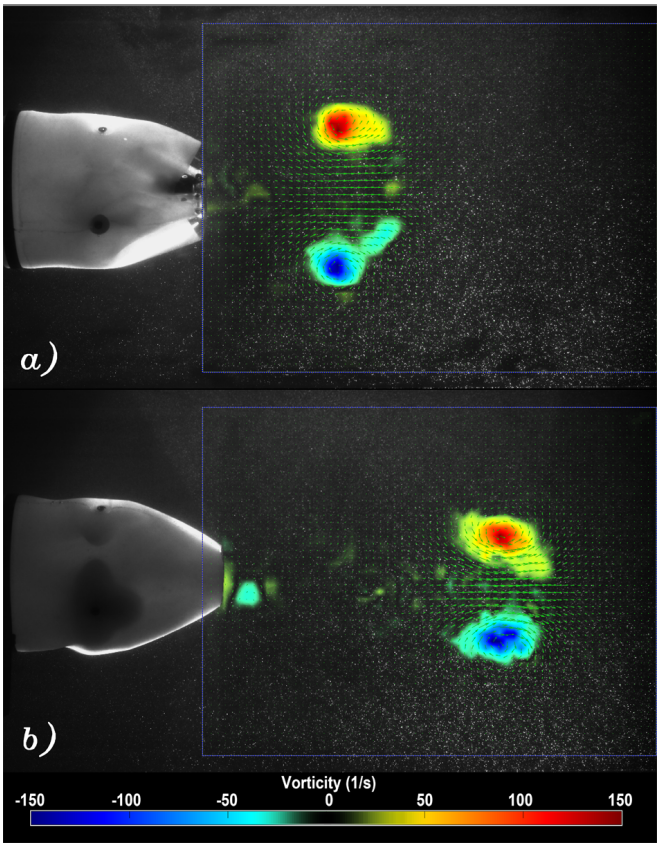

Fig. 7. Mean vorticity ω (n=10) from PIV analysis behind design *I* (a) and *II* (b) at $t = 0.5$ s. Arrows indicate velocity and direction of flow and blue and red regions (vorticity) denote clockwise and counterclockwise rotation.

and downstream vortex ring along the y-axis [20], [21]:

$$\Gamma = \oint \vec{u} dy = \int_{-\infty}^{+\infty} \vec{u} dy = \int_{-y(u_y \approx 0)}^{+y(u_y \approx 0)} \vec{u} dy \qquad (7)$$

The circulation was measured by integration of the tangent velocity component on a circular path around the vortex core for circular paths with increasing radius. The path with the maximum circulation was selected for the momentum and force calculation. Momentum p_v of the vortex ring could then be calculated from fluid density ρ, circulation Γ and the vortex ring area given by radius r, i.e. half the distance between the two vortices:

$$p_v = \rho \Gamma \pi r^2 \qquad (8)$$

The PIV analysis shows (Fig. 7) a distinct formation of a vortex ring behind the underwater thrust device for design *I* and *II* at the same time ($t = 0.5$ s); after start of the closing motion. Design *I* (Fig. 7, a) shows a vortex ring with a larger diameter and a slower exit velocity than design *II* (Fig. 7, b). In Fig. 8, the measured momentum as the force integral over pulse time (Δt = 0.14 to 0.16 s) is compared against the averaged momentum of the fluid particles from PIV measurements. For the force measurements, this implies that only the positive thrust component was considered. The comparison in momentum of both designs shows a 15-16 %

higher momentum for design *I* in a single pulse (Fig. 8). This relative difference is consistent in both methods (thrust measurement and PIV calculation). However, the momentum calculations with the PIV method are 20% lower than those of the thrust measurements. This can be expected, since the PIV method inherently includes the negative thrust at the end of a pulse, by averaging the momentum of the fluid particles in the control volume. It is also likely that the real vortex formation differs from the idealized ring model, leading to an underestimation in momentum. The volume of the ring vortex of design *I* is larger than that of design *II*, what is expected to be responsible for the higher thrust, even under a lower exhaust velocity. Moreover, the force measurements for design *II* show curves with two peaks, but both are below the one peak of the design *I* force curve, which thus also shows a higher mean force.

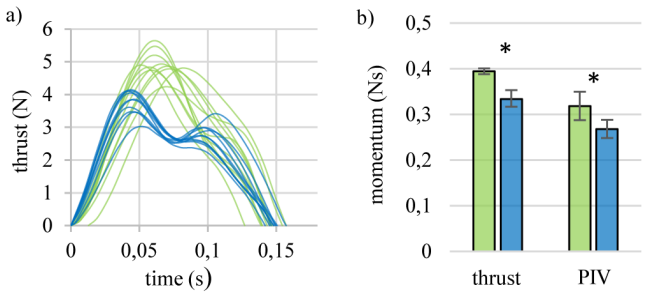

Fig. 8. Results of measured thrust (a) and momentum based on thrust measurements and PIV data (b) for a closing movement of design *I* (green) and *II* (blue), measured ($n = 10$) and from PIV -calculation ($n = 10$). Both methods show statistically higher momentum for design *I* (*: one-way ANOVA, $P < 0.001$).

V. CONCLUSION AND FUTURE PERSPECTIVE

A novel design for a combined rigid-soft underwater thruster device has been discussed in this work, followed by a simplified thrust model and a detailed investigation of the fluid dynamics. Combining classical rigid-body linkages for actuation with soft structures allows for the effective designs of underwater jetting devices. Precise and truthful models of fluid and coupled structural dynamics are non-trivial to establish and costly to compute. However, we show that by simple considerations and approximations to thrust can be obtained. This modeling can be useful in the development of similar apparatuses. Experiments have shown the validity of our computations and that we have achieved effective vortex creation. The vortex shedding at the end of each pulse deserves a broader insight to decrease negative and increase overall thrust. In terms of control, actuation frequencies close to the *eigenmodes* of the system are expected to enhance thrusting performance. Next to improved water ingestion by different passive valves or altered mantle mechanics, a thrust vectoring can also be opted by changing the linkage geometry during movements. This can make the device steerable and it could therefore be redesigned to an untethered swimming device.

ACKNOWLEDGMENT

Funded by the Deutsche Forschungsgemeinschaft (DFG, German Research Foundation) - 404971005. We thank Prof. Dr. Kesel of the Biomimetics-Innovation-Centre, City University of Applied Sciences, Bremen for the collaboration and support.

REFERENCES

[1] E. W. Hawkes, C. Majidi, M.T. Tolley, "Hard questions for soft robotics", *Science Robotics*, vol. 6, no. 53, 2021
[2] R. Salazar, A. Campos, V. Fuentes, A. Abdelkefi, "A review on the modeling, materials, and actuators of aquatic unmanned vehicles", *Ocean Engineering*, vol. 172, pp. 257–285, 2019
[3] M. Krieg, K. Mosheni, "Dynamic Modeling and Control of Biologically Inspired Vortex Ring Thrusters for Underwater Robot Locomotion", *IEEE Trans. on Robotics*, vol. 26, no. 3, 2010
[4] M. Krieg, K. Mosheni, "Thrust Characterization of a Bioinspired Vortex Ring Thruster for Locomotion of Underwater Robots", *IEEE Journal of Oceanic Engineering*, vol. 33, no. 2, 2008
[5] F. G. Serchi, A. Arienti, I. Baldoli, C. Laschi, "An elastic pulsed-jet thruster for Soft Unmanned Underwater Vehicles", *IEEE ICRA*, pp. 5103–5110, 2013
[6] F. G. Serchi, A. Arienti, C. Laschi, "Biomimetic Vortex Propulsion: Toward the New Paradigm of Soft Unmanned Underwater Vehicles", *IEEE Trans. on Mechatronics*, vol. 18, no. 2, 2013
[7] F. Renda, F. G. Serchi, F. Boyer, C. Laschi, "Structural Dynamics of a Pulsed-Jet Propulsion System for Underwater Soft Robots", *Int. J. of Adv. Rob. Systems*, vol. 12, no. 68, 2015
[8] X. Bi, Q. Zhu, "Fluid-structure investigation of a squid-inspired swimmer", *Physics of Fluids*, vol. 31, no. 10, 2019
[9] F. Gao, Z. Wang, Y. Wang, Y. Wang, J. Li, "A Prototype of a Biomimetic Mantle Jet Propeller Inspired by Cuttlefish Actuated by SMA Wires and a Theoretical Model for its Jet Thrust", *J. of Bionic Engineering*, vol. 11, pp. 412–422, 2014
[10] S. Iacoponi, G. Picardi, M. Chellapurath, M. Calisti, C. Laschi, "Underwater soft jet propulsion based on a Hoberman mechanism", *IEEE RoboSoft*, pp. 449–454, 2018
[11] T. Bujard, F. G. Serchi, G. D. Weymouth, "A resonant squid-inspired robot unlocks biological propulsive efficiency", *Science Robotics*, vol. 6, no. 50, 2021
[12] E. J. Anderson, M. Demont, "The mechanics of locomotion in the squid Loligo pealei: locomotory function and unsteady hydrodynamics of the jet and intramantle pressure", *Journal of Experimental Biology*, vol. 203, pp. 2851–2863, 2000
[13] P. F. Linden, J. S. Turner, "Optimal vortex rings and aquatic propulsion mechanisms", *Proc. R. Soc. B Biol. Sci*, vol. 271, no. 1539, pp. 647–653, 2004
[14] J. H. Costello, S. P. Colin, J. O. Dabiri, B. J. Gemmell, K. N. Lucas, K. R. Sutherland, "The Hydrodynamics of Jellyfish Swimming" *Annu. Rev. Mar. Sci*, vol. 13, pp. 5.1–5.22, 2021
[15] I. K. Bartol, P. S. Krueger, W. J. Stewart, J. T. Thompson, "Hydrodynamics of pulsed jetting in juvenile and adult brief squid Lolliguncula brevis: evidence of multiple jet 'modes and their implications for propulsive efficiency", *J. Exp. Biol.*, vol. 212, no. 12, pp. 1889–1903, 2009
[16] N. El-Atab et al, "Soft Actuators for Soft Robotic Applications: A Review", *Adv. Intel. Sys.*, vol. 2, no. 10, 2020
[17] A. del Río ,"Biologically inspired actuation mechanism for an aquatic soft robot", *B.S. thesis, Hochschule Bremen, Bremen, Germany*, 2021
[18] W.G. Gladfelter, "A comparative analysis of the locomotory systems of medusoid Cnidaria", *Helgoländer wiss. Meeresunters.*, vol. 25, pp. 228–272, 1973
[19] W. Thielicke, R. Sonntag, "Particle Image Velocimetry for MATLAB: Accuracy and enhanced algorithms in PIVlab", *J. Open Res. Softw.*, vol. 9, no. 1, pp. 1–14, 2021
[20] E. J. Stamhuis, S. Nauwelaerts, "Propulsive force calculations in swimming frogs II. Application of a vortex ring model to DPIV data", *J. Exp. Biol.*, vol. 208, no. 8, 2005
[21] W. Thielicke, E. J. Stamhuis, "PIVlab Towards User-friendly, Affordable and Accurate Digital Particle Image Velocimetry in MATLAB", *J. Open Res. Softw.*, vol. 2, no. 1, 2014